Inverse Problems **26** (2010) 035009 (16pp) doi:10.1088/0266-5611/26/3/035009

Compressive inverse scattering: II. Multi-shot SISO measurements with born scatterers

Albert C Fannjiang

Department of Mathematics, University of California, Davis, CA 95616-8633, USA

E-mail: fannjiang@math.ucdavis.edu

Received 17 July 2009, in final form 28 January 2010
Published 19 February 2010
Online at stacks.iop.org/IP/26/035009

Abstract

Inverse scattering methods capable of compressive imaging are proposed and analyzed. The methods employ randomly and repeatedly (multiple-shot) the single-input–single-output (SISO) measurements in which the probe frequencies, the incident, and the sampling directions are related in a precise way and are capable of recovering exactly scatterers of sufficiently low sparsity. For point targets, various sampling techniques are proposed to transform the scattering matrix into the random Fourier matrix. Two schemes are particularly interesting: the first one employs multiple frequencies with the sampling angle always in the back-scattering direction resembling the synthetic aperture (SA) imaging; the second employs only single frequency with the sampling angle in the (nearly) forward-scattering direction in the high-frequency limit, resembling the setting of x-ray tomography. The results for point targets are then extended to the case of localized extended targets by interpolating from grid points. In particular, an explicit error bound is derived for the piece-wise constant interpolation which is shown to be a practical way of discretizing localized extended targets and enabling the compressed sensing techniques. For distributed extended targets, the Littlewood–Paley basis is used in analysis. A specially designed sampling scheme then transforms the scattering matrix into a block-diagonal matrix with each block being the random Fourier matrix corresponding to one of the multiple dyadic scales of the extended target. In other words, by the Littlewood–Paley basis and the proposed sampling scheme the different dyadic scales of the target are decoupled and therefore can be reconstructed scale-by-scale by the proposed method. Moreover, with probes of any single frequency ω the coefficients in the Littlewood–Paley expansion for scales up to $\omega/(2\pi)$ can be exactly recovered.

(Some figures in this article are in colour only in the electronic version)

1. Introduction

Consider the scattering of the incident plane wave

$$u^{\mathrm{i}}(\mathbf{r}) = \mathrm{e}^{\mathrm{i}\omega\mathbf{r}\cdot\mathbf{d}} \tag{1}$$

by the variable refractive index $n^2(\mathbf{r}) = 1 + \nu(\mathbf{r})$ where $\mathbf{d}$ is the incident direction. The scattered field satisfies the Lippmann–Schwinger equation [8]

$$u^{\mathrm{s}}(\mathbf{r}) = \omega^2 \int \nu(\mathbf{r}')(u^{\mathrm{i}}(\mathbf{r}') + u^{\mathrm{s}}(\mathbf{r}'))G(\mathbf{r}, \mathbf{r}', \omega)\,\mathrm{d}\mathbf{r}', \qquad \mathbf{r} \in \mathbb{R}^d, \qquad d = 2, 3, \tag{2}$$

where $G(\mathbf{r}, \mathbf{r}', \omega)$ is the Green function of the operator $-(\Delta + \omega^2)$. We assume that the wave speed is unity and hence the frequency equals the wavenumber ω.

The scattered field has the far-field asymptotic

$$u^{\mathrm{s}}(\mathbf{r}) = \frac{\mathrm{e}^{\mathrm{i}\omega|\mathbf{r}|}}{|\mathbf{r}|^{(d-1)/2}}(A(\hat{\mathbf{r}}, \mathbf{d}, \omega) + \mathcal{O}(|\mathbf{r}|^{-1})), \qquad \hat{\mathbf{r}} = \mathbf{r}/|\mathbf{r}|, \tag{3}$$

where A is the scattering amplitude. In inverse scattering theory, the scattering amplitude is the measurement data determined by the formula [8]

$$A(\hat{\mathbf{r}}, \mathbf{d}, \omega) = \frac{\omega^2}{4\pi} \int \mathrm{d}\mathbf{r}' \nu(\mathbf{r}')u(\mathbf{r}')\,\mathrm{e}^{-\mathrm{i}\omega\mathbf{r}'\cdot\hat{\mathbf{r}}}. \tag{4}$$

The main objective of inverse scattering then is to reconstruct the medium inhomogeneities ν from the knowledge of the scattering amplitude. In part I [11] and this paper the target to be imaged consists of a finite number of *point* scatterers. And the main techniques for reconstruction are from the theory of *compressed sensing*. In [11] we analyze the *one, but high, frequency* imaging method with the single-input–multiple-output (SIMO), multiple-input-single output (MISO), and multiple-input–multiple-output (MIMO) measurements in which for every incident plane wave the scattering amplitude is sampled at multiple directions *independent* of the incident wave.

In this paper the focus is on the *multi-shot* single-input–single-output (SISO) measurement in which for every randomly selected incident plane wave the scattering amplitude is sampled at only one direction *correlated* with the incident wave.

Our motivation for this alternative imaging method is practical as well as theoretical. On the theoretical aspect, the analysis of the high-frequency SIMO/MISO and MIMO schemes employs the coherence theory of compressed sensing which deals with only *random* targets under a suitable sparsity constraint. On the other hand, the *multi-shot* SISO method proposed in this paper is amenable to the restricted isometry theory of the random Fourier matrix which guarantees reconstruction for *all* targets under the weakest known sparsity constraint. On the practical aspect, the present method can achieve a comparable performance with a much lower frequency or bandwidth (figure 7). Moreover, the case of *extended* targets can be treated by either interpolating from grid points or using the wavelet basis in this approach. The main drawback, though, of the present approach, in comparison to that of [11], is that the multiple scattering effect is not accounted for.

In section 2, we discuss the case of point scatterers and propose several sampling schemes to transform the scattering matrix into the random Fourier matrix which is amenable to the compressed sensing techniques. One scheme employs multiple frequencies with the sampling angle always in the back-scattering direction resembling the synthetic aperture (SA) imaging; another scheme employs only a single frequency with the sampling angle in the (nearly) forward-scattering direction in the high-frequency limit, resembling the setting of x-ray tomography. We then extend these results to the case of localized extended targets by

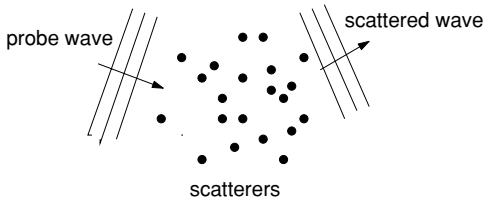

Figure 1. Far-field imaging of discrete scatterers.

interpolating from grid points in section 3. In section 4 we analyze the case of distributed extended targets using the Littlewood–Paley basis and propose a sampling scheme to block-diagonolize the scattering matrix. Each block is in the form of a random Fourier matrix and corresponds to one dyadic scale of the target. Hence, our method has the capability of imaging the target scale-by-scale by the compressed sensing techniques. Moreover, the coefficients in the Littlewood–Paley expansion for scales up to $\omega/(2\pi)$ can be exactly recovered by using probes of any single frequency ω. We numerically test these sampling methods and compare their success probabilities in section 5. We conclude and comment on the issue of resolution in section 6.

2. Point scatterers

For the simplicity of notation, we will focus on two dimensions below (see also figure 1).

We consider the medium with point scatterers located in a square lattice

$$\mathcal{L} = \{\mathbf{r}_i = (x_i, z_i) : i = 1, \ldots, m\}$$

of spacing ℓ. The total number m of grid points in $\mathcal{L}$ is a perfect square. Without loss of generality, assume $x_j = j_1\ell$, $z_j = j_2\ell$ where $j = (j_1-1)\sqrt{m}+j_2$ and $j_1, j_2 = 1, \ldots, \sqrt{m}$. Let ν_j, $j = 1, \ldots, m$, be the strength of the scatterers. Let $\mathcal{S} = \left\{\mathbf{r}_{i_j} = \left(x_{i_j}, z_{i_j}\right) : j = 1, \ldots, s\right\}$ be the locations of the scatterers. Hence, $\nu_j = 0, \forall \mathbf{r}_j \notin \mathcal{S}$.

For the discrete medium the scattering amplitude becomes a finite sum:

$$A(\hat{\mathbf{r}}, \mathbf{d}, \omega) = \frac{\omega^2}{4\pi} \sum_{j=1}^{m} \nu_j u(\mathbf{r}_j)\, \mathrm{e}^{-\mathrm{i}\omega \mathbf{r}_j \cdot \hat{\mathbf{r}}}. \tag{5}$$

Unlike [11] which covers both linear and nonlinear scattering, here we work exclusively under the Born approximation in which the exciting field $u(\mathbf{r}_j)$ is replaced by the incident field $u^{\mathrm{i}}(\mathbf{r}_j)$; unlike [11] which deals exclusively with one frequency, here we will work with multiple frequencies.

Let $\mathbf{d}_l, \hat{\mathbf{r}}_l, l = 1, \ldots, n$, be various incident and sampling directions for the frequencies $\omega_l, l = 1, \ldots, n$, to be determined later. Define the measurement vector $Y = (Y_l) \in \mathbb{C}^n$ with

$$Y_l = \frac{4\pi}{\omega^2} A(\hat{\mathbf{r}}_l, \mathbf{d}_l, \omega_l), \qquad l = 1, \ldots, n. \tag{6}$$

The measurement vector is related to the target vector $X = (\nu_j) \in \mathbb{C}^m$ by the sensing matrix $\mathbf{\Phi}$ as $Y = \mathbf{\Phi} X$. Let $\theta_l, \tilde{\theta}_l$ be the polar angles of $\mathbf{d}_l, \hat{\mathbf{r}}_l$, respectively. The (l, j)-entry of $\mathbf{\Phi} \in \mathbb{C}^{n\times m}$ is

$$\mathrm{e}^{-\mathrm{i}\omega_l \hat{\mathbf{r}}_l \cdot \mathbf{r}_j}\, \mathrm{e}^{\mathrm{i}\omega_l \mathbf{d}_l \cdot \mathbf{r}_j} = \mathrm{e}^{\mathrm{i}\omega_l \ell (j_2(\sin\theta_l - \sin\tilde{\theta}_l) + j_1(\cos\theta_l - \cos\tilde{\theta}_l))}, \qquad j = (j_1 - 1) + j_2. \tag{7}$$

Note that the all entries of Φ have unit modulus. As in [11] we reconstruct X as the solution of the L^1-minimization, called basis pursuit (BP):

$$\min \|Z\|_1, \qquad \text{s.t.} \quad \Phi Z = Y \tag{8}$$

which can be solved by a linear program or by various greedy algorithms [1, 7, 16].

In the presence of noise/error E of size ε as in

$$Y = \Phi X + E, \qquad \|E\|_2 \leqslant \varepsilon, \tag{9}$$

(8) is replaced by the relaxation scheme called the basis pursuit denoising (BPDN):

$$\min\|Z\|_1, \qquad \text{s.t.} \qquad \|Y - \Phi Z\|_2 \leqslant \epsilon. \tag{10}$$

A fundamental notion in compressed sensing under which BP yields the unique exact solution is the restrictive isometry property (RIP) due to Candès and Tao [5]. Precisely, let the sparsity s of a vector $Z \in \mathbb{C}^m$ be the number of nonzero components of Z and define the restricted isometry constant δ_s to be the smallest positive number such that the inequality

$$\kappa(1-\delta_s)\|Z\|_2^2 \leqslant \|\Phi Z\|_2^2 \leqslant \kappa(1+\delta_s)\|Z\|_2^2$$

holds for all $Z \in \mathbb{C}^m$ of sparsity at most s and some constant $\kappa > 0$. For the target vector X let $X^{(s)}$ denote the best s-sparse approximation of X in the sense of the L^1-norm, i.e.

$$X^{(s)} = \operatorname{argmin}\|Z - X\|_1, \quad \text{s.t.} \quad \|Z\|_0 \leqslant s$$

where $\|Z\|_0$ denotes the number of nonzero components, called the sparsity, of Z. Clearly, $X^{(s)}$ consists of the s largest components of X.

Now we state the fundamental result of the RIP approach [2] which is an improvement of the results of [3, 5].

Proposition 1 [2]**.** *Suppose the restricted isometry constant of* Φ *satisfies the inequality*

$$\delta_{2s} < \sqrt{2} - 1 \tag{11}$$

with $\kappa = 1$. *Then the solution* $\hat{X}$ *of BPDN (10) satisfies*

$$\|\hat{X} - X\|_2 \leqslant C_1 s^{-1/2}\|X - X^{(s)}\|_1 + C_2\varepsilon \tag{12}$$

for some constants C_1 *and* C_2.

Remark 1. For general $\kappa \neq 1$, one can consider the normalized version of (9)

$$\frac{1}{\sqrt{\kappa}}Y = \frac{1}{\sqrt{\kappa}}\Phi X + \frac{1}{\sqrt{\kappa}}E$$

by which it follows that

$$\|\hat{X} - X\|_2 \leqslant C_1 s^{-1/2}\|X - X^{(s)}\|_1 + C_2\frac{\varepsilon}{\sqrt{\kappa}}. \tag{13}$$

We wish to write the (l, j)-entry of the sensing matrix in the form

$$\mathrm{e}^{\mathrm{i}\pi(j_1\xi_l + j_2\zeta_l)}, \qquad j = (j_1 - 1)\sqrt{m} + j_2, \qquad j_1, j_2 = 1, \ldots, \sqrt{m}, \quad l = 1, \ldots, n, \tag{14}$$

where ξ_l, ζ_l are independently and uniformly distributed in $[-1, 1]$ in view of the following theorem.

Proposition 2 [14]**.** *Suppose*

$$\frac{n}{\ln n} \geqslant C\delta^{-2}\sigma \ln^2\sigma \ln m \ln\frac{1}{\alpha}, \qquad \alpha \in (0, 1), \tag{15}$$

for a given sparsity σ where C is an absolute constant. Then the restricted isometry constant of the matrix with entry (14) satisfies

$$\delta_\sigma \leqslant \delta$$

with $\kappa = n$ and with the probability at least $1-\alpha$.

See [3, 6, 15] for the case when ξ_l, ζ_l belong to the discrete subset of $[-1, 1]$ of equal spacing $2/\sqrt{m}$.

To construct a sensing matrix of the form (14) we proceed as follows. Write (ξ_l, ζ_l) in the polar coordinates ρ_l, ϕ_l as

$$(\xi_l, \zeta_l) = \rho_l(\cos\phi_l, \sin\phi_l), \qquad \rho_l = \sqrt{\xi_l^2 + \zeta_l^2} \leqslant \sqrt{2} \tag{16}$$

and set

$$\omega_l(\cos\theta_l - \cos\tilde{\theta}_l) = \sqrt{2}\rho_l\Omega\cos\phi_l$$
$$\omega_l(\sin\theta_l - \sin\tilde{\theta}_l) = \sqrt{2}\rho_l\Omega\sin\phi_l$$

where Ω is a parameter to be determined later (30). Equivalently, we have

$$-\sqrt{2}\omega_l \sin\frac{\theta_l - \tilde{\theta}_l}{2}\sin\frac{\theta_l + \tilde{\theta}_l}{2} = \Omega\rho_l\cos\phi_l \tag{17}$$

$$\sqrt{2}\omega_l \sin\frac{\theta_l - \tilde{\theta}_l}{2}\cos\frac{\theta_l + \tilde{\theta}_l}{2} = \Omega\rho_l\sin\phi_l. \tag{18}$$

This set of equations determines the single-input-(θ_l, ω_l)–single-output-$\tilde{\theta}_l$ mode of sampling.

The following implementation of (17)–(18) is natural. Let the sampling angle $\tilde{\theta}_l$ be related to the incident angle θ_l via

$$\theta_l + \tilde{\theta}_l = 2\phi_l + \pi, \tag{19}$$

and set the frequency ω_l to be

$$\omega_l = \frac{\Omega\rho_l}{\sqrt{2}\sin\frac{\theta_l - \tilde{\theta}_l}{2}}. \tag{20}$$

Then the entries (7) of the sensing matrix $\mathbf{\Phi}$ have the form

$$\mathrm{e}^{\mathrm{i}\sqrt{2}\Omega\ell(j_1\xi_l + j_2\zeta_l)}, \qquad l = 1, \ldots, n, \qquad j_1, j_2 = 1, \ldots, \sqrt{m}. \tag{21}$$

By the square symmetry of the problem, it is clear that relation (19) can be generalized to

$$\theta_l + \tilde{\theta}_l = 2\phi_l + \eta\pi, \quad \eta \in \mathbb{Z}. \tag{22}$$

On the other hand, the symmetry of the square lattice should not play a significant role and hence we expect the result to be insensitive to any *fixed* $\eta \in \mathbb{R}$, independent of l, as long as (20) holds. Indeed this is confirmed by numerical simulations below (figure 5).

Let us focus on three specific measurement schemes.

Scheme I. This scheme employs Ω-band limited probes, i.e. $\omega_l \in [-\Omega, \Omega]$. This and (20) lead to the constraint

$$\left|\sin\frac{\theta_l - \tilde{\theta}_l}{2}\right| \geqslant \frac{\rho_l}{\sqrt{2}}. \tag{23}$$

The simplest way to satisfy (19) and (23) is to set

$$\phi_l = \tilde{\theta}_l = \theta_l + \pi, \tag{24}$$

$$\omega_l = \frac{\Omega\rho_l}{\sqrt{2}}, \tag{25}$$

$l = 1, \ldots, n$. In this case the scattering amplitude is always sampled in the back-scattering direction. This resembles the synthetic aperture imaging which has been previously analyzed under the paraxial approximation in [13]. In contrast, the forward-scattering direction with $\tilde{\theta}_l = \theta_l$ almost surely violates the constraint (23).

Scheme II. This scheme employs single-frequency probes not less than Ω:

$$\omega_l = \gamma\Omega, \qquad \gamma \geqslant 1, \qquad l = 1, \ldots, n. \tag{26}$$

To satisfy (22) and (20) we set

$$\theta_l = \phi_l + \frac{\eta\pi}{2} + \arcsin\frac{\rho_l}{\gamma\sqrt{2}} \tag{27}$$

$$\tilde{\theta}_l = \phi_l + \frac{\eta\pi}{2} - \arcsin\frac{\rho_l}{\gamma\sqrt{2}} \tag{28}$$

with $\eta \in \mathbb{Z}$. The difference between the incident angle and the sampling angle is

$$\theta_l - \tilde{\theta}_l = 2\arcsin\frac{\rho_l}{\gamma\sqrt{2}} \tag{29}$$

which diminishes as $\gamma \to \infty$. In other words, in the high-frequency limit, the sampling angle approaches the incident angle. This resembles the setting of the x-ray tomography.

Scheme III. This scheme employs probes of unlimited frequency band. Let θ_l be n arbitrary distinct numbers in $[-\pi, \pi]$ and let $\tilde{\theta}_l$ and ω_l be determined by (22) and (20), respectively. The possibility of having a small divisor in (20) renders the bandwidth unlimited in principle.

The following result is an immediate consequence of propositions 1 and 2.

Theorem 1. *Let ξ_l, ζ_l be independently and uniformly distributed in $[-1, 1]$ and let (ρ_l, ϕ_l) be the polar coordinates of (ξ_l, ζ_l), i.e.*

$$(\xi_l, \zeta_l) = \rho_l(\cos\phi_l, \sin\phi_l).$$

Let the probe frequencies ω_l, the incident angles θ_l and the sampling angles $\tilde{\theta}_l$ satisfy (19) and (20), for example, by scheme I, II or III.

Suppose

$$\Omega\ell = \pi/\sqrt{2} \tag{30}$$

and suppose (15) holds with $\sigma = 2s$ and any $\delta < \sqrt{2} - 1$. Then (11) with $\kappa = n$ is satisfied for the matrix $\mathbf{\Phi}$ and the bound (13) holds true with the probability at least $1 - \alpha$.

3. Localized extended targets

In this section we consider extended targets that are localized in space (see figure 2). We represent such targets by interpolating from grid points and thus extend the preceding results for point targets to localized extended targets. We will treat the case of distributed extended targets that are not localized in space in the next section.

Suppose that the target function $\nu(\mathbf{r})$ is continuous and has a compact support. Consider the filtered version ν_η of ν:

$$\nu_\eta(\mathbf{r}) = \int g_\eta(\mathbf{r} - \mathbf{r}')\nu(\mathbf{r}')\,\mathrm{d}\mathbf{r}' \tag{31}$$

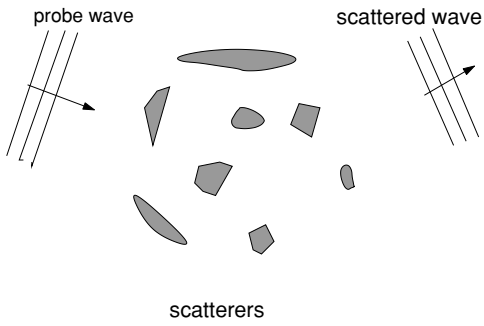

Figure 2. Scattering from extended targets.

where $g_\eta(\mathbf{r}) = \eta^{-2} g(\mathbf{r}/\eta)$ for any integrable filter function g such that $\int g(\mathbf{r})\,\mathrm{d}\mathbf{r} = 1$. Clearly, ν_η tends to ν as $\eta \to 0$.

Next we discretize (31) by replacing the integral by the Riemann sum of step size ℓ. We obtain

$$\nu_{\eta,\ell}(\mathbf{r}) = \ell^2 \sum_{\mathbf{p}\in I} g_\eta(\mathbf{r} - \ell\mathbf{q})\nu(\ell\mathbf{q}), \qquad I \subset \mathbb{Z}^2, \tag{32}$$

which is as smooth as the interpolation element g_η.

Since ν has a compact support, I is a finite set. For simplicity let I be the square sublattice

$$I = \{\mathbf{q} = (q_1, q_2) : q_1, q_2 = 1, \ldots, \sqrt{m}\}$$

of total cardinality m. Let $j = (q_1 - 1)\sqrt{m} + q_2$. Define the target vector $X = (X_j) \in \mathbb{C}^m$ with $X_j = \nu(\ell\mathbf{q})$. Let ω_l and $\mathbf{d}_l$ be the probe frequencies and directions, respectively, and let $\hat{\mathbf{r}}_l$ be the sampling directions for $l = 1, \ldots, n$. Now we write the data vector Y in form (9) with the sensing matrix elements

$$\begin{aligned}\Phi_{lj} &= \frac{1}{2\pi\,\hat{g}(\eta\omega_l(\mathbf{d}_l - \hat{\mathbf{r}}_l))} \int_{\mathbb{R}^2} g_\eta(\mathbf{r}' - \ell\mathbf{q})\, \mathrm{e}^{\mathrm{i}\omega_l(\mathbf{d}_l - \hat{\mathbf{r}}_l)\cdot\mathbf{r}'}\,\mathrm{d}\mathbf{r}', \qquad j = (q_1 - 1)\sqrt{m} + q_2 \\ &= \mathrm{e}^{\mathrm{i}\omega_l \ell\mathbf{q}\cdot(\mathbf{d}_l - \hat{\mathbf{r}}_l)}\end{aligned} \tag{33}$$

and the error term E due to the filtered discretization. For sufficiently small η, ℓ we may assume $\|E\|_2 \leqslant \varepsilon n^{1/2}$ for a given $\varepsilon > 0$ (see remark 1 and below).

The crucial observation is that the sensing matrix (33) is identical to (7) with $(x_j, z_j) = \omega\mathbf{q}$ and any *isotropic* filter function g. Therefore, theorem 1 holds verbatim for the case of localized extended targets formulated above.

How small must η and ℓ be in order to ensure that $\|E\|_2 \leqslant \varepsilon n^{1/2}$? This can be answered roughly as follows. First, by the inequality $\|E\|_2 \leqslant \|E\|_\infty \sqrt{n}$ it suffices to have $\|E\|_\infty \leqslant \varepsilon$. Now consider the transformation $\mathcal{T}$, defined by

$$(\mathcal{T}\nu)_l = \frac{1}{2\pi\,\hat{g}(\eta\omega_l(\mathbf{d}_l - \hat{\mathbf{r}}_l))} \int \nu(\mathbf{r}')\, \mathrm{e}^{\mathrm{i}\omega_l(\mathbf{d}_l - \hat{\mathbf{r}}_l)\cdot\mathbf{r}'}\,\mathrm{d}\mathbf{r}',$$

from the space of continuous functions supported on $[\ell, m\ell]^2$ to $\mathbb{C}^n$, cf (4). By definition

$$E = \mathcal{T}\nu - \mathcal{T}\nu_{\eta,\ell}$$

and we have

$$\|E\|_\infty \leqslant \frac{\|\nu - \nu_{\eta,\ell}\|_1}{2\pi \min_l |\hat{g}(\eta\omega_l(\mathbf{d}_l - \hat{\mathbf{r}}_l))|}.$$

For the sampling schemes I and II (with $\gamma = 1$) of section 2, we can give an explicit bound for the discretization error

$$\|E\|_\infty \leqslant \frac{1}{2\pi}\|\nu - \nu_{\eta,\ell}\|_1 \|\hat{g}^{-1}\|_{L^\infty([-\eta\ell^{-1}\pi,\eta\ell^{-1}\pi]^2)},$$

where $\|\cdot\|_{L^\infty([-\eta\ell^{-1}\pi,\eta\ell^{-1}\pi]^2)}$ denotes the L^∞-norm of functions defined on $[-\eta\ell^{-1}\pi, \eta\ell^{-1}\pi]^2$.

Theorem 2. *Consider the sampling schemes I and II (with $\gamma = 1$) of section 2. Assume (30) and*

$$\|\nu - \nu_{\eta,\ell}\|_1 \leqslant \frac{2\pi\varepsilon}{\|\hat{g}^{-1}\|_{L^\infty([-\eta\ell^{-1}\pi,\eta\ell^{-1}\pi]^2)}}. \tag{34}$$

Suppose that (15) holds with $\sigma = 2s$ and any $\delta < \sqrt{2} - 1$. Then the bound (13) with $\kappa = n$ holds true with the probability at least $1 - \alpha$.

Remark 2. For example, consider the smooth isotropic filter function

$$g(\mathbf{r}) = \frac{1}{2\pi}\,\mathrm{e}^{-\frac{|\mathbf{r}|^2}{2}}$$

with $\hat{g}(\mathbf{k}) = g(\mathbf{k})$. With the choice $\eta = \ell$, condition (34) can be formulated as

$$\|\nu - \nu_{\ell,\ell}\|_1 \leqslant \mathrm{e}^{-\pi^2/2}\varepsilon. \tag{35}$$

For another example, consider the indicator function g on the unit square $\left[-\frac{1}{2}, \frac{1}{2}\right]^2$. The resulting interpolation is the piece-wise constant approximation. Then

$$\hat{g}(k_1, k_2) = \frac{2}{\pi} \cdot \frac{\sin\frac{k_1}{2}}{k_1} \cdot \frac{\sin\frac{k_2}{2}}{k_2}.$$

Setting again $\eta = \ell$ we obtain the condition

$$\|\nu - \nu_{\ell,\ell}\|_1 \leqslant \frac{4}{\pi^2}\varepsilon \tag{36}$$

which appears to be much more useful than (35) because of the larger constant in (36).

4. Distributed extended targets

In this section, we consider extended targets represented by square-integrable functions $\nu(x, z)$.

To this end we use the Littlewood–Paley basis

$$\hat{\psi}(\xi, \zeta) = \begin{cases} (2\pi)^{-1}, & \pi \leqslant |\xi|, |\zeta| \leqslant 2\pi \\ 0, & \text{otherwise} \end{cases} \tag{37}$$

or

$$\psi(\mathbf{r}) = (\pi^2 xz)^{-1}(\sin(2\pi x) - \sin(\pi x)) \cdot (\sin(2\pi z) - \sin(\pi z)). \tag{38}$$

Then the set of functions

$$\psi_{\mathbf{p},\mathbf{q}}(\mathbf{r}) = 2^{-(p_1+p_2)/2}\psi(2^{-\mathbf{p}}\mathbf{r} - \mathbf{q}), \quad \mathbf{p}, \mathbf{q} \in \mathbb{Z}^2, \tag{39}$$

with

$$2^{-\mathbf{p}}\mathbf{r} = (2^{-p_1}x, 2^{-p_2}z),$$

forms an orthonormal wavelet basis in $L^2(\mathbb{R}^2)$ [10]. In terms of the Littlewood–Paley basis we have the expansion

$$\nu(x, z) = \sum_{\mathbf{p},\mathbf{q}\in\mathbb{Z}^2} \nu_{\mathbf{p},\mathbf{q}}\psi_{\mathbf{p},\mathbf{q}}(x, z). \tag{40}$$

With the incident fields

$$u_k^{\mathrm{i}}(\mathbf{r}) = \mathrm{e}^{\mathrm{i}\omega_k \mathbf{r}\cdot\mathbf{d}_k}, \qquad k = 1, \ldots, n,$$

we have from (4), (6) and (40) that

$$Y_k = 2\pi \sum_{\mathbf{p},\mathbf{q}\in\mathbb{Z}^2} 2^{(p_1+p_2)/2} v_{\mathbf{p},\mathbf{q}}\, \mathrm{e}^{\mathrm{i}\omega_k 2^{\mathbf{p}}(\mathbf{d}_k-\hat{\mathbf{r}}_k)\cdot\mathbf{q}} \hat{\psi}(\omega_k 2^{\mathbf{p}}(\hat{\mathbf{r}}_k - \mathbf{d}_k)), \quad k = 1, \ldots, n. \tag{41}$$

Define the sensing matrix elements to be

$$\Phi_{k,l} = \frac{1}{2n_{\mathbf{p}}+1} \hat{\psi}(\omega_k 2^{\mathbf{p}}(\hat{\mathbf{r}}_k - \mathbf{d}_k))\, \mathrm{e}^{\mathrm{i}\omega_k 2^{\mathbf{p}}(\mathbf{d}_k-\hat{\mathbf{r}}_k)\cdot\mathbf{q}} \tag{42}$$

and let $\mathbf{\Phi} = [\Phi_{k,l}]$, where $\mathbf{d}_k$, $\hat{\mathbf{r}}_k$, ω_k are given below.

Let

$$l = \sum_{j_1=-p_*}^{p_1-1} \sum_{j_2=-p_*}^{p_2-1} (2m_{\mathbf{j}}+1)^2 + (q_1+m_{\mathbf{p}})(2m_{\mathbf{p}}+1) + (q_2+m_{\mathbf{p}}+1),$$
$$|\mathbf{q}|_\infty \leqslant m_{\mathbf{p}}, \qquad |\mathbf{p}|_\infty \leqslant p_*,$$
$$k = \sum_{j_1=-p_*}^{p_1'-1} \sum_{j_2=-p_*}^{p_2'-1} (2n_{\mathbf{j}}+1)^2 + (q_1'+n_{\mathbf{p}'})(2n_{\mathbf{p}'}+1) + (q_2'+n_{\mathbf{p}'}+1),$$
$$|\mathbf{q}'|_\infty \leqslant n_{\mathbf{p}'}, \qquad |\mathbf{p}'|_\infty \leqslant p_*,$$

for some $m_{\mathbf{p}}$, $n_{\mathbf{p}}$, $p_* \in \mathbb{N}$, be the column and row indices, respectively, of $\mathbf{\Phi}$. It is important to keep in mind how k and l are related to $(\mathbf{p}', \mathbf{q}')$ and $(\mathbf{p}, \mathbf{q})$, respectively, in order to understand the scheme described below.

Let ξ_k, ζ_k be independent, uniform random variables on $[-1, 1]$ and define

$$\alpha_k = \frac{\pi}{\omega_k 2^{p_1'}} \cdot \begin{cases} 1+\xi_k, & \xi_k \in [0,1] \\ -1+\xi_k, & \xi_k \in [-1,0] \end{cases} \tag{43}$$

$$\beta_k = \frac{\pi}{\omega_k 2^{p_2'}} \cdot \begin{cases} 1+\zeta_k, & \zeta_k \in [0,1] \\ -1+\zeta_k, & \zeta_k \in [-1,0] \end{cases}. \tag{44}$$

Suppose $\alpha_k, \beta_k \in [-1, 1]$ for all $\mathbf{p}'$, $|\mathbf{p}'| \leqslant p_*$. This holds true, for example, when the frequencies ω_k satisfy the constraint

$$\omega_k 2^{p_1'} \geqslant 2\pi, \qquad \omega_k 2^{p_2'} \geqslant 2\pi. \tag{45}$$

Let (ρ_k, ϕ_k) be the polar coordinates of (α_k, β_k).

As before, let $\theta_k, \tilde{\theta}_k$ be the angles of incidence and sampling, respectively, which are chosen according to

$$-2\sin\frac{\theta_k-\tilde{\theta}_k}{2}\sin\frac{\theta_k+\tilde{\theta}_k}{2} = \alpha_k = \rho_k\cos\phi_k \tag{46}$$

$$2\sin\frac{\theta_k-\tilde{\theta}_k}{2}\cos\frac{\theta_k+\tilde{\theta}_k}{2} = \beta_k = \rho_k\sin\phi_k \tag{47}$$

in analogy with (17)–(18). This means

$$-\omega_k 2^{\mathbf{p}}(\hat{\mathbf{r}}_k - \mathbf{d}_k) = \omega_k(2^{p_1}\alpha_k, 2^{p_2}\beta_k) = \pi(2^{p_1-p_1'}(\mathrm{sgn}(\xi_k)+\xi_k), 2^{p_2-p_2'}(\mathrm{sgn}(\zeta_k)+\zeta_k)). \tag{48}$$

By (48) and the definition of $\hat{\psi}$ it is clear that $\Phi_{k,l}$ are zero if $\mathbf{p} \neq \mathbf{p}'$. Consequently, the sensing matrix is the block-diagonal matrix with each block (indexed by $\mathbf{p} = \mathbf{p}'$) in the form of random Fourier matrix:

$$\Phi_{k,l} = \frac{1}{2n_{\mathbf{p}}+1} \mathrm{e}^{\mathrm{i}\pi(q_1\xi_k + q_2\zeta_k)}. \tag{49}$$

Let $X = (X_l)$ with

$$X_l = 2\pi(2n_{\mathbf{p}}+1)2^{(p_1+p_2)/2}\nu_{\mathbf{p},\mathbf{q}}$$

be the target vector. Let

$$m = \sum_{j_1=-p_*}^{p_*} \sum_{j_2=-p_*}^{p_*} (2m_{\mathbf{j}}+1)^2.$$

We can then write the measurement vector $Y = \mathbf{\Phi} X$ where $\mathbf{\Phi} \in \mathbb{C}^{n\times m}$. The above observation means that the target structures of different dyadic scales are decoupled and can be determined separately by our approach using compressed sensing techniques.

To solve (46)–(47) we consider

$$\theta_k + \tilde{\theta}_k = 2\phi_k + \pi \tag{50}$$

and

$$2\sin\frac{\theta_k - \tilde{\theta}_k}{2} = \rho_k. \tag{51}$$

To satisfy relationships (50) and (51) we set

$$\theta_k = \phi_k + \frac{\pi}{2} + \arcsin\frac{\rho_k}{2} \tag{52}$$

$$\tilde{\theta}_k = \phi_k + \frac{\pi}{2} - \arcsin\frac{\rho_k}{2} \tag{53}$$

analogous to (27) and (28).

In the case of extreme anisotropy (needle-like structure), say $2^{p_1-p_2} \gg 1$, (43)–(44) implies

$$\phi_k \approx \pm\frac{\pi}{2}$$

and hence

$$\theta_k + \tilde{\theta}_k \approx 0 \tag{54}$$

by (50). On the other hand, if $2^{p_1-p_2} \ll 1$, then

$$\phi_k \approx \pm\pi$$

and hence

$$\theta_k + \tilde{\theta}_k \approx \pi. \tag{55}$$

Relations (54) and (55) are reminiscent of Snell's law of reflection if $\tilde{\theta}_k$ are interpreted as the reflection angles.

Using the RIP for the random Fourier matrix of each block, we obtain the following theorems analogous to theorem 1.

Theorem 3. *For each* $\mathbf{p}$, $|\mathbf{p}| \leqslant p_*$, *let (15) be satisfied for* $n = n_{\mathbf{p}}$ *and* $\sigma = 2s_{\mathbf{p}}$ *and any* $\delta < \sqrt{2}-1$. *Suppose*

$$\omega_k \geqslant 2\pi \cdot 2^{\max(p_1,p_2)}, \qquad k = 1,\ldots,n_{\mathbf{p}}. \tag{56}$$

Let ξ_l, ζ_l *be independently and uniformly distributed in* $[-1,1]$. *Let the incident and sampling angles be determined by (43)–(44), (46)–(47).*

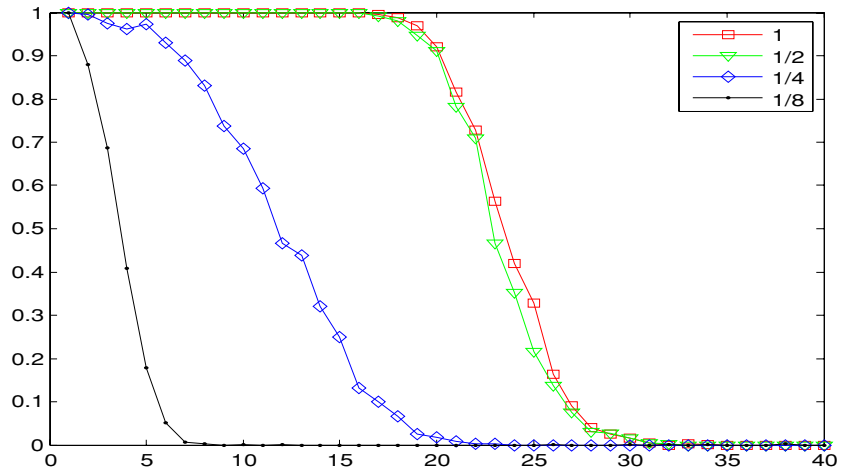

Figure 3. Success probabilities for scheme I with (58). The label indicates the value of η. As the recipe (24) is increasingly violated, the performance degrades accordingly.

Then (11) is satisfied for the $\mathbf{p}$*-block of the sensing matrix with the probability at least* $1-\alpha$*. Consequently, the solution* $\hat{X}_{\mathbf{p}}$ *by BP (10) satisfies*

$$\|\hat{X}_{\mathbf{p}} - X_{\mathbf{p}}\|_2 \leqslant C_1 s_{\mathbf{p}}^{-1/2} \left\| X_{\mathbf{p}} - X_{\mathbf{p}}^{(s_{\mathbf{p}})} \right\|_1 + C_2 \varepsilon \tag{57}$$

for the same constants C_1, C_2 *as in (13).*

Remark 3. Condition (56) implies that the wavelengths are not larger than the scales under interrogation, consistent with the classical resolution criterion.

Theorem 3 allows reconstruction with probes of single sufficiently high-frequency $\omega_k = \omega^{\#}$:

$$\omega^{\#} \geqslant \pi 2^{1+p_*}.$$

The beauty of the theorem, however, lies in the fact that with probes of any frequency ω the coefficients in the Littlewood–Paley expansion for scales up to $\omega/(2\pi)$ can be recovered (exactly in the absence of noise).

5. Numerical results

Greedy algorithms have significantly lower computational complexity than linear programming and have provable performance under various conditions. For example, under the condition $\delta_{3s} < 0.06$ the subspace pursuit (SP) algorithm is guaranteed to exactly recover X via a finite number of iterations [9]. We have used SP for reconstruction in all our simulations with the following parameters: $m = 2500, \ell = 1, \Omega = \pi/\sqrt{2}, n = 100$. The probability of recovery is calculated by using 1000 independent runs. In figures 3–7, the vertical axis is for the probability of recovery and the horizontal axis is for the number of point scatterers.

To test scheme I numerically, we use (25) and

$$\tilde{\theta}_l = \theta_l + \eta\pi, \qquad \eta = 1, 1/2, 1/4, 1/8, \tag{58}$$

to see if the deviations from (24) have any impact on performance. Their probabilities of recovery are plotted as a function of the sparsity in figure 3. Clearly, the performance

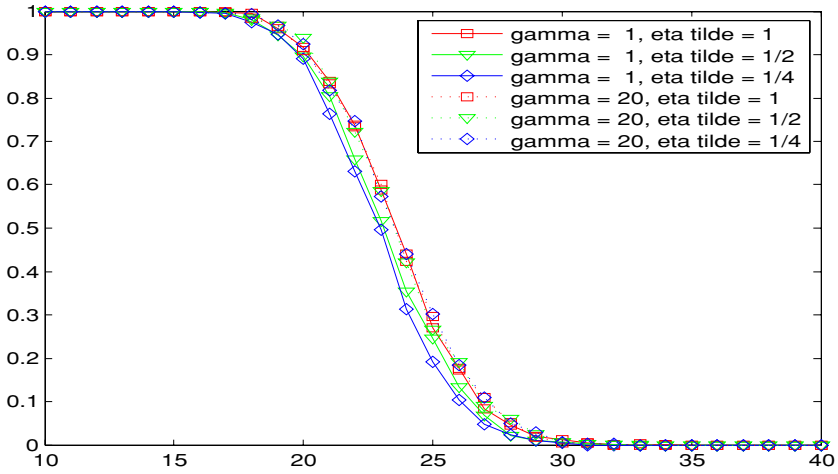

Figure 4. Success probabilities for scheme II: (a) $\eta = 1$, $\tilde{\eta} = 1, 1/2, 1/4$ with $\gamma = 1, 20$.

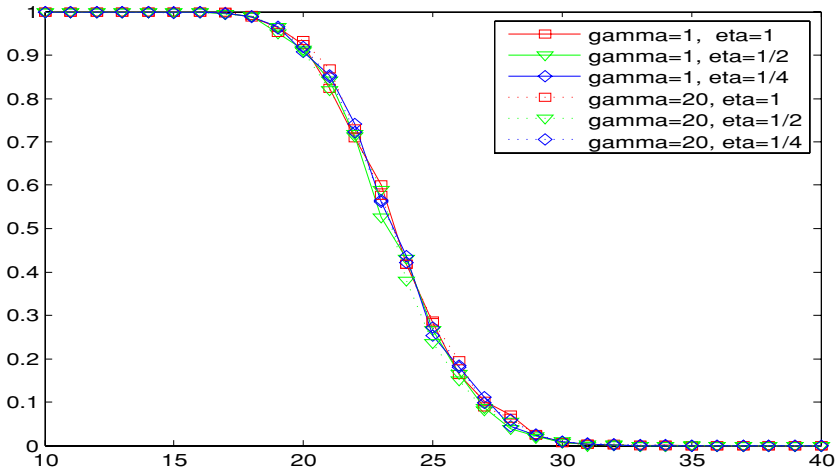

Figure 5. Success probabilities for schemes II: (b) $\eta = \tilde{\eta} = 1, 1/2, 1/4$ with $\gamma = 1, 20$.

deteriorates rapidly as the difference between the sampling and incident angles decreases. This is due to increasingly more frequent and more severe violation of (23) as a result. In other words, the backward-scattering direction is the optimal sampling direction for scheme I.

Likewise, to test scheme II numerically, we use (26),

$$\tilde{\theta}_l = \phi_l + \frac{\tilde{\eta}\pi}{2} - \arcsin\frac{\rho_l}{\gamma\sqrt{2}}, \qquad \tilde{\eta} = 1, 1/2, 1/4, \tag{59}$$

instead of (28), and (27) with (a) $\eta = 1$ as well as with (b) $\eta = \tilde{\eta} = 1, 1/2, 1/4$. Condition (29) is satisfied if and only if $\eta = \tilde{\eta}$.

The results for case (a) at $\gamma = 1, 20$ are shown in figure 4 and the results for case (b) with $\eta = \tilde{\eta}$ at $\gamma = 1, 20$ are displayed in figure 5. The slight degradation in performance for

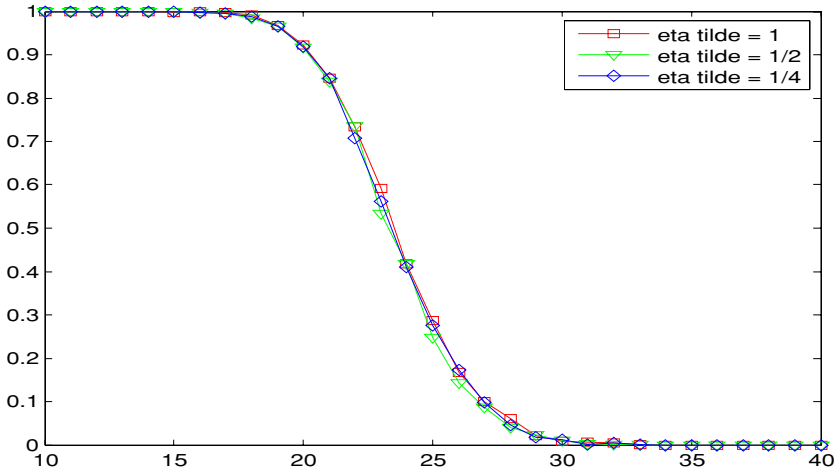

Figure 6. Success probabilities for scheme III with (60).

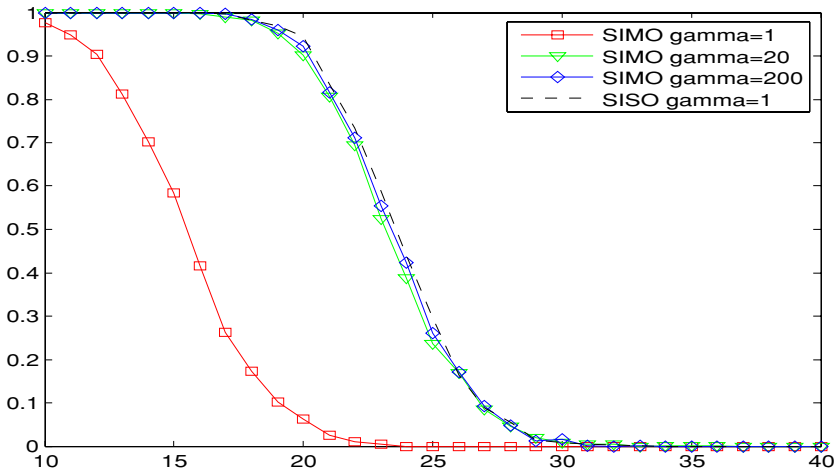

Figure 7. Solid curves are the success probabilities for the SIMO measurement at $\gamma = 1, 20, 200$ and the dashed curve is the SISO scheme II at $\gamma = 1$.

e.g. $\eta = 1, \tilde{\eta} = 1/4, \gamma = 1$ results from the violation of (29) (and hence (23)) which affects the performance significantly for small γ. For large γ, it has been shown in [11] that the sampling angles can be chosen independently of the incident angles to maintain a high level of performance (figure 7). On the other hand, when (29) holds, the performance is essentially independent of both γ and $\tilde{\eta}$, figure 5.

For scheme III we use equally spaced incident angles $\theta_l \in [\pi/6, \pi/3]$, (20) and

$$\theta_l + \tilde{\theta}_l = 2\phi_l + \tilde{\eta}\pi, \qquad \tilde{\eta} = 1, 1/2, 1/4. \tag{60}$$

As shown in figure 6, the performance is essentially independent of $\tilde{\eta}$.

We demonstrate numerically the high-frequency SIMO schemes analyzed in [11] and compare their performance with that of the multi-shot SISO schemes presented above. A case in point would be to use (26) and (28) but for a fixed incident angle, say $\theta_l = 0, \forall l$ (in

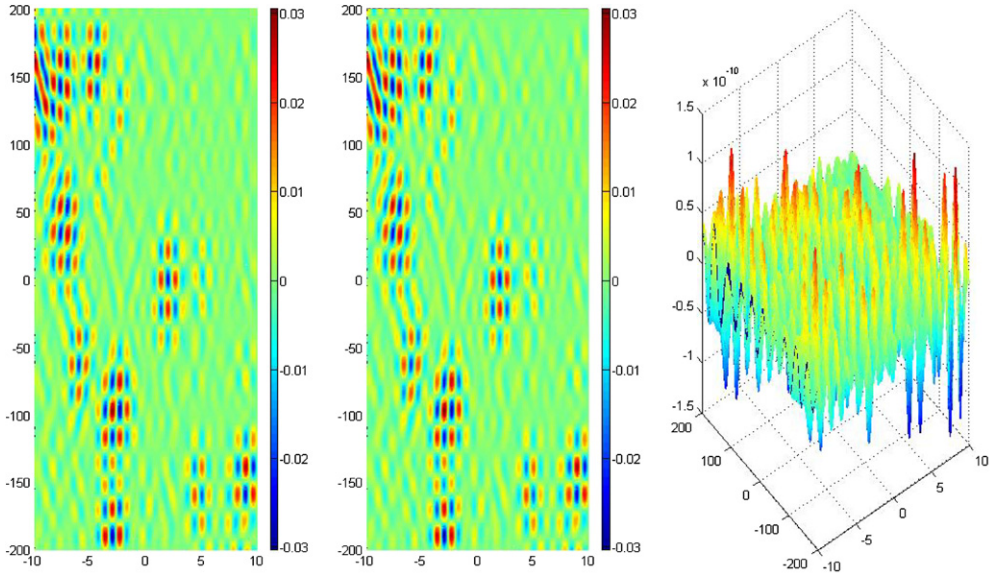

Figure 8. Imaging of an extended target of the scales $(1, 32)$. The left plot is the exact structure; the middle plot is the the reconstructed profile; the right plot shows the (round-off) error. See the color bars for the meaning of the color code (see online).

this case (29) is almost certainly violated). In [11] it is established that the SIMO schemes with sampling angles, *independent of the incident angles*, achieves a high performance in reconstructing a sparse target with a sufficiently high-frequency probe wave (i.e. $\gamma \gg 1$). The success probabilities of the SIMO schemes for $\gamma = 1, 20, 200$ are calculated and plotted in figure 7. Consistent with the theory [11], the low frequency case with $\gamma = 1$ has the worst performance. Clearly the performance of the SIMO schemes improves with γ and in the limit $\gamma \gg 1$ approaches that of the multi-shot SISO scheme II. There is a negligible difference between the performances for $\gamma = 20$ and $\gamma = 200$ both of which follow closely that of the SISO scheme II with $\gamma = 1$ (black dashed line in figure 7).

Finally we demonstrate the reconstruction with the Littlewood–Paley basis. Since the scattering matrix is block-diagonalized by the proposed sampling schemes (43)–(44) and (46)–(47), we consider targets of a single pair of dyadic scales. In this simulation, the reconstruction is carried out for a target on the scales $(1, 32)$ ($\mathbf{p} = (0, 5)$) with 42 nonzero coefficients ($s_{\mathbf{p}} = 42$) among 441 possible modes ($m_{\mathbf{p}} = 10, 21$ modes in each coordinate) by using 81 samples ($n_{\mathbf{p}} = 81$). The target and its reconstruction in the domain $[-10, 10] \times [-200, 200]$ are color-coded (see online) and displayed in figure 8.

6. Conclusion and discussion

We have proposed, analyzed and numerically tested several multi-shot SISO sampling schemes which transform the scattering matrix into the random Fourier matrix in the case of point and localized extended scatterers and the block-diagonal form of random Fourier matrices in the case of distributed extended targets.

In the case of point scatterers, these sampling schemes are either multi-frequency band limited (I) or single frequency outside band (II). For scheme I , the sampling direction is the backward direction analogous to the synthetic aperture radar (SAR) while for scheme II in the

high-frequency limit the optimal sampling is in the forward direction, analogous to the x-ray tomography. Both schemes produce nearly the same recovery probability with the resolution given by (30), i.e.

$$\ell = \frac{\pi}{\sqrt{2}\Omega}.$$

We have extended this approach to the case of localized extended targets by interpolating from grid points. We have formulated the approximate scheme as inversion with noisy data. In particular, we have derived an explicit error bound for the simple piece-wise constant interpolation.

In the case of distributed extended targets, the block-diagonal form of the scattering matrix in the Littlewood–Paley representation means that different dyadic scales of the target are decoupled and can be imaged scale-by-scale separately by our method. Moreover, we can determine the coefficients in the Littlewood–Paley expansion (40) for scales up to $\omega/(2\pi)$ by using probes of any single frequency ω. The disadvantage of the Littlewood–Paley basis is that a localized target has slowly decaying coefficients and hence is not compressible in this basis.

The SIMO schemes in which the scattered field of an incident angle is measured at multiple sampling angles have been studied in [11–13]. Except for the special case of the periodic scatterers lying on a transverse plane [12], it is not known if the sensing matrices of the SIMO schemes in general satisfy the RIP or not. In this case, the approach based on the notion of incoherence is taken to analyze the SIMO schemes [11, 13]. This approach is generally more flexible and should be applicable to the SISO schemes considered here.

The main advantage of the SIMO schemes is that in the one-shot setting (one incident field) the inverse scattering problem can be solved exactly *without* the Born approximation by inverting an auxiliary nonlinear system of equations [11]. We are working to extend the idea to the imaging methods with multi-shot measurements.

On the other hand, the SISO schemes with the RIP tend to have a better performance which can be matched by that of the SIMO schemes only at a high frequency as demonstrated in figure 7. In the high-frequency regime the sampling angles can be chosen independently of the incident angles [11].

Acknowledgments

The research is partially supported by the NSF grant DMS-0908535. I thank my students Hsiao-Chieh Tseng (figures 3–7) and Wenjing Liao (figure 8) for preparing the figures.

References

[1] Bruckstein A M, Donoho D L and Elad M 2009 From sparse solutions of systems of equations to sparse modeling of signals *SIAM Rev.* **51** 34–81
[2] Candès E J 2008 The restricted isometry property and its implications for compressed sensing *C. R. Acad. Sci., Paris* I **346** 589–92
[3] Candès E J, Romberg J and Tao T 2006 Robust uncertainty principles: exact signal reconstruction from highly incomplete frequency information *IEEE Trans. Inform. Theory* **52** 489–509
[4] Candès E J, Romberg J and Tao T 2006 Stable signal recovery from incomplete and inaccurate measurements *Commun. Pure Appl. Math.* **59** 1207–23
[5] Candès E J and Tao T 2005 Decoding by linear programming *IEEE Trans. Inform. Theory* **51** 4203–15
[6] Candès E J and Tao T 2006 Near-optimal signal recovery from random projections: universal encoding strategies? *IEEE Trans. Inform. Theory* **52** 54–6-5425
[7] Chen S S, Donoho D L and Saunders M A 2001 Atomic decomposition by basis pursuit *SIAM Rev.* **43** 129–59

[8] Colton D and Kress R 1998 *Inverse Acoustic and Electromagnetic Scattering Theory* 2nd edn (Berlin: Springer)
[9] Dai W and Milenkovic O 2008 Subspace pursuit for compressive sensing: closing the gap between performance and complexity arXiv:0803.0811
[10] Daubechies I 1992 *Ten Lectures on Wavelets* (Philadelphia: SIAM)
[11] Fannjiang A 2010 Compressive inverse scattering: I. High frequency SIMO/MISO and MIMO measurements *Inverse Problems* **26** 035008
[12] Fannjiang A 2009 Compressive imaging of subwavelength structures *SIAM J. Imaging Sci.* **2** 1277–91
[13] Fannjiang A, Yan P and Strohmer T 2009 Compressed remote sensing of sparse objects arXiv:0904.3994
[14] Rauhut H 2008 Stability results for random sampling of sparse trigonometric polynomials *IEEE Trans. Inform. Theor.* **54** 5661–70
[15] Rudelson M and Vershynin R 2008 On sparse reconstruction from Fourier and Gaussian measurements *Commun. Pure Appl. Math.* **111** 1025–45
[16] Temlyakov V N 2008 Greedy approximations *Acta Numer.* **17** 235–409